doi.org/10.26434/chemrxiv.11671806.v1

Phosphonate Metal-Organic Frameworks: A Novel Family of Semiconductors

Konrad Siemensmeyer, Craig A. Peeples, Patrik Tholen, Bünyemin Çoşut, Gabriel Hanna, Gündoğ Yücesan

Submitted date: 21/01/2020 • Posted date: 22/01/2020

Citation information: Siemensmeyer, Konrad; Peeples, Craig A.; Tholen, Patrik; Çoşut, Bünyemin; Hanna, Gabriel; Yücesan, Gündoğ (2020): Phosphonate Metal-Organic Frameworks: A Novel Family of Semiconductors. ChemRxiv. Preprint. https://doi.org/10.26434/chemrxiv.11671806.v1

Herein is reported the first semiconducting and magnetic phosphonate metal-organic framework (MOF), TUB75, which contains a one-dimensional inorganic building unit composed of a zig-zag chain of corner-sharing copper dimers. The solid-state UV-Vis spectrum of TUB75 reveals the existence of a narrow band gap of 1.4 eV, which agrees well with the 1.77 eV one obtained from DFT calculations. Magnetization measurements show that TUB75 is composed of antiferromagnetically coupled copper dimer chains. Due to their rich structural chemistry and exceptionally high thermal/chemical stabilities, phosphonate MOFs like TUB75 may open new vistas in engineerable electrodes for supercapacitors.

File list (1)

Phosphonate metal-organic frameworks: A novel family of semiconductors

Konrad Siemensmeyer, Craig A. Peeples, Patrik Tholen, Bünyemin Çoşut, Gabriel Hanna, Gündoğ Yücesan**

Dr. K. Siemensmeyer Author 1

Helmholtz-Zentrum, Berlin, 14109, Germany

C. A. Peeples Author 2, Prof. G. Hanna Author 5

University of Alberta, Edmonton, T6G 2R3, Canada

E-mail: gabriel.hanna@ualberta.ca

P. Tholen Author 3, Prof. G. Yücesan Author 6

Technische Universität, Berlin, 13355, Germany

E-mail: yuecesan@tu-berlin.de

B. Çoşut Author 4

Gebze Technical University, Gebze, 41400, Turkey

Keywords: Semiconductive MOFs; Magnetic MOFs; DFT calculations; Electrodes; Supercapacitors

Herein is reported the first semiconducting and magnetic phosphonate metal-organic framework (MOF), TUB75, which contains a one-dimensional inorganic building unit composed of a zig-zag chain of corner-sharing copper dimers. The solid-state UV-Vis spectrum of TUB75 reveals the existence of a narrow band gap of 1.4 eV, which agrees well with the 1.77 eV one obtained from DFT calculations. Magnetization measurements show that TUB75 is composed of antiferromagnetically coupled copper dimer chains. Due to their rich structural chemistry and exceptionally high thermal/chemical stabilities, phosphonate MOFs like TUB75 may open new vistas in engineerable electrodes for supercapacitors.

Metal organic frameworks (MOFs) emerged as a new family of microporous materials at the beginning of the 21st century.[1-5] They are composed of inorganic building units (IBUs) and

organic linkers, which combine to create microporous frameworks.[1,3,6,7] Owing to the vast range of organic linker geometries and functional groups, and the option of post-synthetic modification of pore surfaces,[8-10] many diverse applications of MOF chemistry have emerged, including small molecule storage,[11] greenhouse gas sequestration,[12] drug delivery,[13,14] and detoxifying agents[15]; and the presence of IBUs has led to applications in heterogeneous catalysis,[16,17] magnetism,[18-21] and conductivity.[21,22] Among these applications, magnetic MOFs have recently attracted a great deal of attention due to the possibility of creating tunable magnetic materials by varying the host-guest interactions at pore sites or exploiting structural changes induced by MOF breathing; and conductive MOFs are expected to serve as next-generation porous electrode materials with higher and customizable surface areas compared to active carbon electrodes.[21-23]

Traditional MOFs have primarily relied on molecular IBUs known widely as paddle wheel patterns.[1-3] To synthesize magnetic MOFs based on molecular IBUs, the IBUs must be close enough to each other to generate the desired magnetic interactions. The design patterns for such magnetic MOFs have been summarized in two recent review articles.[18,19] Typically, shorter linkers such as CN or azolate linkers make magnetic interactions possible between the inorganic components.[24,25] Also, linkers that can generate free radicals may be used to create magnetically significant MOFs.[26,27] However, because MOF chemistry has evolved towards the use of longer organic linkers for larger surface areas, the distances between the molecular IBUs has increased and thereby diminished the possibility of constructing magnetic MOFs with molecular IBUs.[28] Thus, new architectural strategies for synthesizing magnetic MOFs are in need. Along these lines, one-dimensional (1D) and two-dimensional (2D) IBUs can provide a more suitable platform for magnetic interactions as the metal centers may come into close proximity to each other in such geometries.[29-31] MOFs, which are synthesized at high temperatures and under hydrothermal reaction conditions, usually form 1D chain IBUs.[32-34] In

contrast, conventional MOFs, which are synthesized at low temperatures in the presence of organic solvents,[1-6] usually form molecular IBUs. One-dimensional magnetic chains are well known,[29] but relatively few porous magnetic MOFs with 1D IBUs have been reported in the literature.[18,19,25,31,35]

The construction of conductive MOFs requires more subtle design elements. For example, highly conjugated linkers such as phthalocyanine or porphyrins with ortho-diimine, ortho-dihydroxy, and azolate metal-binding units connected via molecular IBUs composed of a single metal ion, are known to give rise to conductivity.[21-23] However, due to the limited number of metal-binding modes for the single nitrogen and oxygen donating linkers and the highly conservative nature of metal binding in these systems, progress in the design of conductive MOFs has been limited. Alternative metal binding units capable of yielding both rich structural diversity and conductivity are needed for constructing next-generation conductive MOFs.[34,36]

Phosphonate MOFs are known for their high structural diversity due to the multiple metal-binding modes and protonation states of the phosphonic acid group.[37] They are known to contain complex molecular clusters and 1D/2D IBUs.[30,33-36] Recently, Yücesan *et al.* synthesized the phosphonate MOF TUB75 (where TUB stands for Technische Universität Berlin) at temperatures above 180°C and under hydrothermal reaction conditions.[38] The crystal structure revealed that this MOF contains 1D copper dimer chains linked by polyaromatic 1,4-naphthalenediphosphonic acid linkers (see **Figure 1**). This chain structure is unique compared to that of previously reported 1D IBUs in the literature with respect to the presence of three different (and relatively short) characteristic Cu-Cu distances along the 1D IBU (see **Figure 1**B).[30,33-36] As seen in **Figure 1**B, TUB75 is composed of zig-zag copper dimer chains (one of which is portrayed in **Figure 1**B; the experimental and calculated Cu-Cu distances are given in Figure S2 and Table S1, respectively). Its surface area was previously

measured to be 132.1 m^2/g.[38] The thermal decomposition patterns of phosphonate MOFs constructed using 4,4'-bipyridine as the auxiliary linker with 1,4-naphthalenediphosphonic acid, 2,6-naphthalendiphosphonic acid, and different aromatic phosphonic acids were also previously reported.[38,39] MOFs in this family have a general tendency to be thermally stable up to ~375 °C, after which thermal decomposition begins. In our previous work with 2,6-naphthalendiphosphonic acid, we found that removing the 4,4'-bipyridines to obtain pure metal phosphonates increases the thermal stability to ~400 °C.[37] As seen in **Figure 1**B, all of the 1,4-naphthalenediphosphonic acids in TUB75 are fully deprotonated, which leads to substantial electron delocalization within the 1D IBU (see electronic population analyses in Table S2 of the Supporting Information).

In light of the above, in this study, we revisit our phosphonate MOF TUB75 to explore its conductive and magnetic properties. As we will discuss below, we find that TUB75 has an indirect band gap of 1.4 eV (based on a Tauc plot of the UV-Vis spectrum), making it a semiconductor. In addition, we find that TUB75 possesses an antiferromagnetic chain-type IBU. Our density functional theory (DFT) calculations of TUB75's band gap, band structure, partial density of states, and relative energies of the ferromagnetic (FM) and antiferromagnetic (AFM) configurations, provide detailed insight into its electronic structure. The details of our calculations, which employed Slater-type orbital (STO) basis sets, can be found in the Computational Details section of the Supporting Information.

In **Figure 3**B, we present a Tauc plot derived from the UV-Vis spectrum (shown in Figure S2) of a sample of pure handpicked (under a microscope) crystals – thin green needles with an average length of 0.5 mm. An optical band gap of 1.4 eV, typical of a semiconductor, was determined by linear extrapolation of an indirect Tauc plot (see **Figure 3**B).[40,41] Previous

reports on electrical conductivity in MOFs have been mainly based on conductance measurements on pellets.[21] However, conductances obtained from pellet-based measurements may sometimes be overrated due to the presence of minute amounts of conductive metal impurities originating from the starting materials.[21-23] Thus, measuring the UV-Vis spectrum of a sample of handpicked crystals and extracting the band gap from a Tauc plot provides an alternative way to gain insight into the conductivity. Such a measurement coupled with DFT calculations can provide a comprehensive picture of the conductivity of a material.[23]

To gain insight into the semiconductive nature of TUB75, we performed DFT calculations, the details of which are provided in the Supporting Information. The density of states calculation yielded a HOMO-LUMO gap of E_g = 1.77 eV, which is in good agreement with the experimental band gap of 1.4 eV. Based on the projected density of states (pDOS) in **Figure 2**, we see that the HOMO-LUMO gap is predominantly due to atomic orbitals associated with the carbon atoms in the π-conjugated 1,4-naphthalenediphosphonic acid (1,4-NDPA) and 4,4'-bipyridine (4,4'-bpy) auxiliary linker groups. It also appears that there is some contribution from the nitrogen orbitals to the LUMO and a very small contribution from the oxygen orbitals to the HOMO. As for copper, there is effectively no contribution from the copper orbitals to the HOMO and LUMO. There is indication of spin dependence in the higher energy virtual orbitals, primarily associated with the copper atoms and smaller contributions coming from carbon, nitrogen, phosphorous, and oxygen. We further projected the carbon pDOS into the individual contributions from the 1,4-NDPA and the 4,4'-bpy carbons (**Figure 3**). This projection reveals that the HOMO and LUMO are spatially separated, with the HOMO localized on the 1,4-NDPA carbons and the LUMO localized on the 4,4'-bpy carbons. In such a case, a photo-excited electron (in the LUMO) would be spatially separated from its hole (in the HOMO).

Next, we report the results of our magnetization measurements on TUB75 in **Figure 4**A (see Supporting Information for the details of the measurements). The magnetization data exhibits a Néel temperature of $T \cong 30$ K (i.e., the temperature corresponding to the maximum magnetization) that increases with increasing field strength, a behavior that is characteristic of a material with AFM correlations (see **Figure 5** for a depiction of the AFM correlations of spins in the geometry-optimized structure). This is corroborated by our DFT-calculated exchange energy (i.e., the energy difference between the AFM and FM configurations) of $E_{ex} = E_{AFM} - E_{FM}$ = -37.3 meV, indicating that the AFM configuration is more stable than the FM one. Moreover, the position of the maximum does not vary with temperature, which is characteristic of the presence of short-range order in the 1D spin chains and is consistent with the zig-zag chains observed in the crystal structure (**Figure 1**B). At 2 K, we observe a non-zero magnetization that increases with increasing field strength and appears to plateau at higher fields; for the lower field strengths, the magnetization initially decreases and then increases with increasing temperature (up to 10 K), while for the higher field strengths the magnetization simply increases with increasing temperature (up to 10 K). The upturn of the magnetization below 10 K (known as a Curie tail) observed for the lower field strengths is suggestive of the presence of a small amount of paramagnetic impurity, e.g., Cu ions that are not embedded in the TUB75 crystal structure.[31] At high temperatures, the magnetization decreases to zero with increasing temperature, as expected (see **Figure 4**A).

Given the underlying 1D chain geometry, we fit our high-temperature (> 30 K) magnetic susceptibility data (**Figure 4**B) to Heisenberg chain and dimer chain models (depicted in **Figure 4**D). As shown in **Figure 4**B, close fits to the data were obtained with coupling constants of J_{chain} = 16.8 K and J' = -22 K for the Heisenberg chain model,[42,43] and coupling constants of J_{dimer} = 54 K and J_{chain} = -2.6 K for the dimer chain model.[44-46] The signs and

magnitudes of the Heisenberg chain coupling constants are consistent with those observed in antiferromagnetically coupled 1D chains, while those of the dimer chain model are suggestive of another type of coupling. The diamagnetic contribution is small in both cases. As the temperature is lowered to 1 K from 30 K, the magnetic susceptibility predicted by the dimer chain model drops rapidly (ultimately to negative values), in contrast with the experimental susceptibility which drops less rapidly and remains positive. On the other hand, the magnetic susceptibility predicted by the Heisenberg chain model drops less rapidly than the experimental susceptibility and remains positive. As mentioned earlier, these deviations may be due to the presence of impurity spins; thus, we fit the low-temperature (< 10 K) magnetic susceptibility data to a field-dependent Brillouin function plus a baseline signal (dotted black line) that is due to the 1D chains. From **Figure 4**B, we see that this combination of functions (with an impurity content of ~8 %, S = 1⁄2 and g = 2) closely fits the low-temperature data. Given that the magnetic susceptibilities of TUB75, the Heisenberg chain, and the dimer chain are positive, positive, and negative, respectively, at very low temperatures (see **Figure 4**B), it appears that its IBU is best described in terms of Heisenberg chains. A Curie-Weiss fit to the high temperature portion of the inverse magnetic susceptibility is shown in **Figure 4C**. All details of the data fitting are given in the Supporting Information.

Finally, in Fig. 6, we present the DFT-calculated spin density iso-surface, focusing on a portion of the IBU in the AFM configuration. The antiparallel spin density along the copper dimer chain is clearly seen and it is delocalized onto the coppers and their nearest-neighbor oxygens and nitrogens. This result suggests that the magnetic behavior of TUB75 is likely dependent on the shared spin density of these three atoms.

Herein, we have reported on the conductive and magnetic properties of the phosphonate MOF, TUB75. With an experimental band gap value of 1.4 eV, TUB75 is the first semiconducting

phosphonate MOF in the literature, paving the way for a new family of semiconductors with an extremely rich structural chemistry. The metal-binding modes of the phosphonic acid group in TUB75 support a 1D IBU composed of a zig-zag copper dimer chain, which was found to be antiferromagnetically coupled. The temperature-dependent magnetic susceptibility data was well fit using a combination of a Heisenberg chain model at higher temperatures and Brillouin functions at very low temperatures. Our experimental measurements were accompanied by DFT calculations, which yielded a band gap of 1.77 eV in good agreement with the experimental one and support the AFM nature of the IBU. Given the high thermal/chemical stabilities of phosphonate MOFs and the innumerous metal-binding modes of phosphonates, our findings suggest that they could be used in next-generation electrodes and supercapacitors capable of withstanding harsh operating conditions. The vast structural diversity of phosphonate MOFs could lead to a new generation of porous materials with engineerable surface areas and magnetic/conductive properties. Currently, we are working on the reticular chemistry of phosphonate MOFs to explore these possibilities.

Supporting Information

Supporting Information is available.

Acknowledgements

We would like to thank Dr. Pradip Pachfule from TU-Berlin for his help with the UV-Vis measurements. **Funding:** Gündoğ Yücesan would like to thank the DFG for funding his work with grant number DFG YU 267/2-1 and DAAD for supporting Prof. Dr. Bünyemin Çoşut's visit to his lab at TU-Berlin. Gabriel Hanna acknowledges support from the Natural Sciences and Engineering Research Council of Canada (NSERC). The DFT calculations were enabled by support provided by WestGrid (www.westgrid.ca) and Compute Canada

(www.computecanada.ca). **Author contributions:** Gündoğ Yücesan created the hypothesis, supervised the project, and wrote, synthesized, and revised the non-computational parts of the manuscript. Patrik Tholen generated the crystal structure figure (Figure 1). Craig Peeples performed the DFT calculations, generated the computational figures/tables, and wrote the initial drafts of the computational parts of the manuscript. Gabriel Hanna supervised the calculations, wrote/revised the computational parts of the manuscript, and performed extensive critical revisions of the entire manuscript. Konrad Siemensmeyer performed the magnetic measurements and wrote the initial drafts of the corresponding methods and results sections. Bünyemin Çoşut prepared the Tauc plot (Figure 3B). Konrad Siemensmeyer and Craig Peeples contributed equally to this work.

References

[1] M. Eddaoudi, J. Kim, N. Rosi, D. Vodak, J. Wachter, M. O'Keeffe, O. M. Yaghi, Systematic design of pore size and functionality in isoreticular MOFs and their application in methane storage. *Science.* **2002**, 295, 469.

[2] H. C. Zhou, J. R. Long, O. M. Yaghi, Introduction to metal-organic frameworks. *Chem. Rev.* **2012**, 112, 673.

[3] O. M. Yaghi, M. O'Keeffe, N. W. Ockwig, H. K. Chae, M. Eddaoudi, J. Kim, Reticular synthesis and the design of new materials. *Nature*. **2003**, 423, 705.

[4] H. Furukawa, K. E. Cordova, M. O'Keeffe, O. M. Yaghi, The chemistry and applications of metal-organic frameworks. *Science.* **2013**, 341, 974.

[5] H.-C. "Joe" Zhou, S. Kitagawa, Metal-organic frameworks (MOFs). *Chem. Soc. Rev.* **2014**, 43, 5415.

[6] M. J. Kalmutzki, N. Hanikel, O. M. Yaghi, Secondary building units as the turning point in the development of the reticular chemistry of MOFs. *Sci. Adv.* **2018**, 4, 1.

[7] A. Schoedel, M. Li, D. Li, M. O'Keeffe, O. M. Yaghi, Structures of metal-organic frameworks with rod secondary building units. *Chem. Rev.* **2016**, 116, 12466.

[8] S. M. Cohen, The postsynthetic renaissance in porous solids. *J. Am. Chem. Soc.* **2017**, 139, 2855.

[9] Z. Wang, S. M. Cohen, Postsynthetic covalent modification of a neutral metal-organic framework. *J. Am. Chem. Soc.* **2007**, 129, 12368.

[10] K. K. Tanabe, S. M. Cohen, Postsynthetic modification of metal-organic frameworks - A progress report. *Chem. Soc. Rev.* **2011**, 40, 498

[11] M. T. Kapelewski, T. Runčevski, J. D. Tarver, H. Z. H. Jiang, K. E. Hurst, P. A. Parilla, A. Ayala, T. Gennett, S. A. Fitzgerald, C. M. Brown, J. R. Long, Record high hydrogen storage capacity in the metal-organic framework Ni_2(*m*-dobdc) at near-ambient temperatures. *Chem. Mater.* **2018**, 30, 8179.

[12] M. Ding, R. W. Flaig, H. L. Jiang, O. M. Yaghi, Carbon capture and conversion using metal-organic frameworks and MOF-based materials. *Chem. Soc. Rev.* **2019**, 48, 2783.

[13] P. Horcajada, R. Gref, T. Baati, P. K. Allan, G. Maurin, P. Couvreur, G. Férey, R. E. Morris, C. Serre, Metal-organic frameworks in biomedicine. *Chem. Rev.* **2012**, 112, 1232.

[14] K. J. Hartlieb, D. P. Ferris, J. M. Holcroft, I. Kandela, C. L. Stern, M. S. Nassar, Y. Y. Botros, J. F. Stoddart, Encapsulation of ibuprofen in CD-MOF and related bioavailability studies. *Mol. Pharm.* **2017**, 14, 1831.

[15] S. Rojas, T. Baati, L. Njim, L. Manchego, F. Neffati, N. Abdeljelil, S. Saguem, C. Serre, M. F. Najjar, A. Zakhama, P. Horcajada, Metal-organic frameworks as efficient

oral detoxifying agents. *J. Am. Chem. Soc.* **2018**, 140, 9581.

[16] M. Ranocchiari, J. A. Van Bokhoven, Catalysis by metal-organic frameworks: Fundamentals and opportunities. *Phys. Chem. Chem. Phys.* **2011**, 13, 6388.

[17] A. Dhakshinamoorthy, Z. Li, H. Garcia, Catalysis and photocatalysis by metal organic frameworks. *Chem. Soc. Rev.* **2018**, 47, 8134.

[18] E. Coronado, G. Mínguez Espallargas, Dynamic magnetic MOFs. *Chem. Soc. Rev.* **2013**, 42, 1525.

[19] G. Mínguez Espallargas, E. Coronado, Magnetic functionalities in MOFs: From the framework to the pore. *Chem. Soc. Rev.* **2018**, 47, 533.

[20] E. Coronado, M. Giménez-Marqués, G. M. Espallargas, L. Brammer, Tuning the magneto-structural properties of non-porous coordination polymers by HCl chemisorption. *Nat. Commun.* **2012**, 3, 1

[21] C. Yang, R. Dong, M. Wang, P. S. Petkov, Z. Zhang, M. Wang, P. Han, M. Ballabio, S. A. Bräuninger, Z. Liao, J. Zhang, F. Schwotzer, E. Zschech, H. H. Klauss, E. Cánovas, S. Kaskel, M. Bonn, S. Zhou, T. Heine, X. Feng, A semiconducting layered metal-organic framework magnet. *Nat. Commun.* **2019**, 10, 1.

[22] L. Sun, M. G. Campbell, M. Dincə, Electrically conductive porous metal-organic frameworks. *Angew. Chemie - Int. Ed.* **2016**, 55, 3566.

[23] D. Sheberla, J. C. Bachman, J. S. Elias, C. J. Sun, Y. Shao-Horn, M. Dincă, Conductive MOF electrodes for stable supercapacitors with high areal capacitance. *Nat. Mater.* **2017**, 16, 220.

[24] S. I. Ohkoshi, H. Tokoro, Photomagnetism in cyano-bridged bimetal assemblies. *Acc. Chem. Res.* **2012**, 45, 1749.

[25] W. Ouellette, A. V. Prosvirin, K. Whitenack, K. R. Dunbar, J. Zubieta, A thermally and hydrolytically stable microporous framework exhibiting single-chain magnetism: Structure and properties of $[Co_2(H_{0.67}bdt)_3]\cdot 20H_2O$. *Angew. Chemie - Int. Ed.* **2009**, 48, 2140.

[26] T. B. Faust, D. M. D'Alessandro, Radicals in metal-organic frameworks. *RSC Adv.* **2017**, 4, 17498.

[27] D. Maspoch, D. Ruiz-Molina, K. Wurst, N. Domingo, M. Cavallini, F. Biscarini, J. Tejada, C. Rovira, J. Veciana, A nanoporous molecular magnet with reversible solvent-induced mechanical and magnetic properties. *Nat. Mater.* **2003**, 2, 190.

[28] O. K. Farha, I. Eryazici, N. C. Jeong, B. G. Hauser, C. E. Wilmer, A. A. Sarjeant, R. Q. Snurr, S. T. Nguyen, A. Ö. Yazaydin, J. T. Hupp, Metal-organic framework materials with ultrahigh surface areas: Is the sky the limit? *J. Am. Chem. Soc.* **2012**, 134, 15016.

[29] G. Yücesan, V. Golub, C. J. O'Connor, J. Zubieta, Temperature dependence of the crystal chemistry of the oxovanadium-ethylenediphosphonate/copper(II)-2,2′-bipyridine system. Crystal structures of the two-dimensional $[Cu(bpy)VO_2(O_3PCH_2CH_2PO_3H)]\bullet 1.5H_2O$ and of the one-dimensional $[Cu(bpy)VO_2(O_3PCH_2CH_2PO_3H)]$. *Solid State Sci.* **2005**, 7, 133.

[30] M. A. AlDamen, S. Cardona-Serra, J. M. Clemente-Juan, E. Coronado, A. Gaita-Ariño, C. Martí-Gastaldo, F. Luis, O. Montero, Mononuclear lanthanide single molecule magnets based on the polyoxometalates $[Ln(W5O_{18})2]9-$ and [Ln(β2-SiW11O39)2]13- (LnIII = Tb, Dy, Ho, Er, Tm, and Yb). *Inorg. Chem.* **2009**, 48, 3467.

[31] D. T. Tran, X. Fan, D. P. Brennan, P. Y. Zavalij, S. R. J. Oliver, Open metal-organic framework containing cuprate chains. *Inorg. Chem.* **2005**, 44, 6192.

[32] K. J. Gagnon, H. P. Perry, A. Clearfield, Conventional and unconventional metal-

organic frameworks based on phosphonate ligands: MOFs and UMOFs. *Chem. Rev.* **2012**, 112, 1034.

[33] M. Taddei, F. Costantino, R. Vivani, Robust metal-organic frameworks based on tritopic phosphonoaromatic ligands. *Eur. J. Inorg. Chem.* **2016**, 4300.

[34] G. Yücesan, Y. Zorlu, M. Stricker, J. Beckmann, Metal-organic solids derived from arylphosphonic acids. *Coord. Chem. Rev.* **2018**, 369, 105.

[35] Y. Zorlu, D. Erbahar, A. Çetinkaya, A. Bulut, T. S. Erkal, A. O. Yazaydin, J. Beckmann, G. Yücesan, A cobalt arylphosphonate MOF-superior stability, sorption and magnetism. *Chem. Commun.* **2019**, 55, 3053.

[36] S. J. I. Shearan, N. Stock, F. Emmerling, J. Demel, P. A. Wright, K. D. Demadis, M. Vassaki, F. Costantino, R. Vivani, S. Sallard, I. R. Salcedo, A. Cabeza, M. Taddei, New directions in metal phosphonate and phosphinate chemistry. *Crystals*. **2019**, 9, 1.

[37] R. A. Coxall, S. G. Harris, D. K. Henderson, S. Parsons, P. A. Tasker, R. E. P. Winpenny, Inter-ligand reactions: In situ formation of new polydentate ligands. *J. Chem. Soc. Dalt. Trans.***2000**, 14, 2349.

[38] A. Bulut, Y. Zorlu, M. Wörle, A. Çetinkaya, H. Kurt, B. Tam, A. Ö. Yazaydın, J. Beckmann, G. Yücesan, Short naphthalene organophosphonate linkers to microporous frameworks. *ChemistrySelect*. **2017**, 2, 7050.

[39] A. Bulut, M. Maares, K. Atak, Y. Zorlu, B. Çoşut, J. Zubieta, J. Beckmann, H. Haase, G. Yücesan, Mimicking cellular phospholipid bilayer packing creates predictable crystalline molecular metal-organophosphonate macrocycles and cages. *CrystEngComm*. **2018**, 20, 2152.

[40] A. R. Zanatta, I. Chambouleyron, Absorption edge, band tails, and disorder of amorphous semiconductors. *Phys. Rev. B.* **1996**, 53, 3833.

[41] J. Tauc, R. Grigorovici, A. Vancu, Optical properties and electronic structure of amorphous germanium. *Phys. Stat. Sol.* **1966**, 15, 627.

[42] W.E. Hatfield, R.R. Weller, J.W. Hall; Exchange coupling in the sulfur-bridged quasi-linear-chain compound bis(dimethyldithiocarbamato)copper(II). Observations on exchange in sulfur-bridged copper(II) compounds, *Inorg. Chem.* **1980**, 19, 3825.

[43] J.C. Bonner, M.E. Fisher; Linear magnetic chains with anisotropic coupling, *Phys. Rev. A.* **1964**, 135, A640.

[44] D. C. Johnston, in *Handbook of Magnetic Materials*, edited by K. H. J. Buschow (Elsevier, The Netherlands, 1997), Vol. 10.

[45] E. S. Klyushina et. al., Hamiltonian of the S=1/2 dimerized antiferromagnetic-ferromagnetic quantum spin chain $BaCu_2V_2O_8$, *Phys. Rev. B*. **2018**, 98, 104413.

[46] S. Eggert et al., Susceptibility of the spin 1/2 Heisenberg antiferromagnetic chain, *Phys. Rev. Lett.* **1994**, 73, 332.

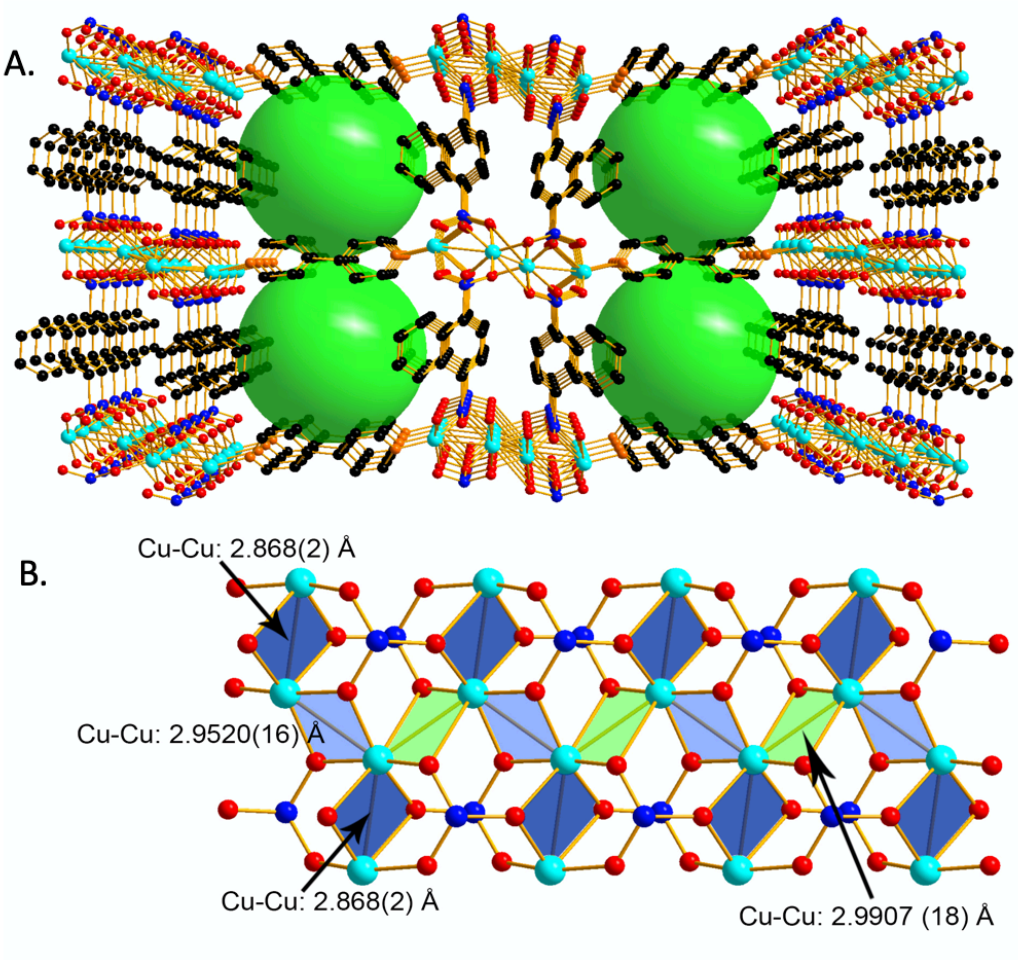

Figure 1. A) One layer of the [{Cu_2(4,4'-bpy)$_{0.5}$}(1,4-NDPA)] (TUB-75) MOF, showing nine 1D copper dimer IBUs and four void channels (which extend into and out of plane). **B)** Side view of the 1D IBU consisting of a zig-zag chain of corner-sharing copper dimers, with Cu-Cu distances of less than 3 Å. Dimers are colored based on their Cu-Cu bond distances. Color definitions: O – red; N – orange; Cu – cyan; C – black; P – blue.

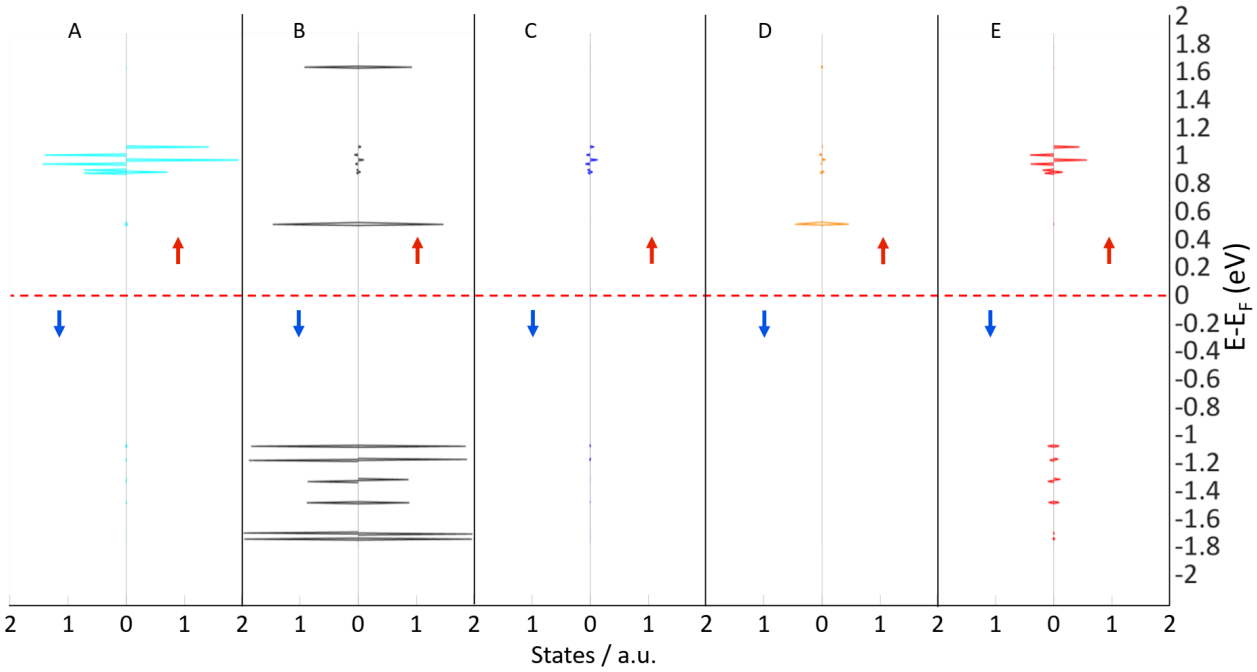

Figure 2. Spin-up and spin-down projected density of states for TUB75 in the AFM configuration. (A) Copper, (B) Carbon, (C) Nitrogen, (D) Phosphorous, (E) Oxygen.

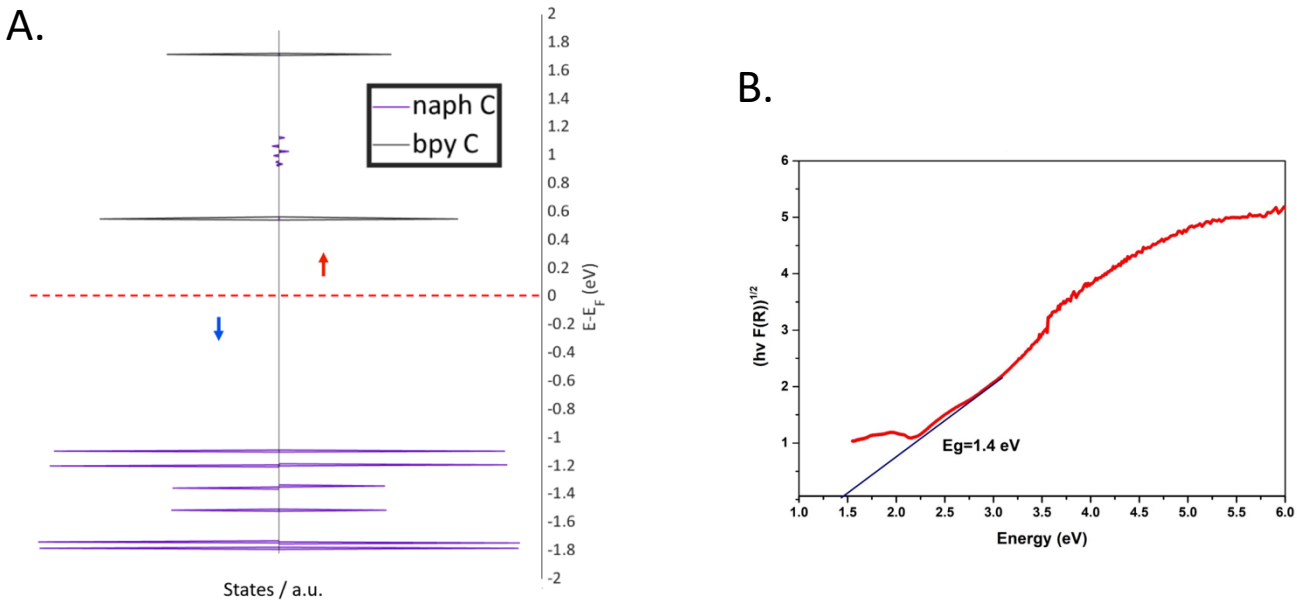

Figure 3. A) Spin-up and spin-down projected density of states of the 1,4-NDPA and 4,4'-bpy carbons for TUB75 in the AFM configuration. B) Indirect Tauc plot derived from the UV-Vis absorption spectrum of TUB75 (shown in Figure S2), revealing a typical semiconductor pattern and a band gap of E_g = 1.4 eV.

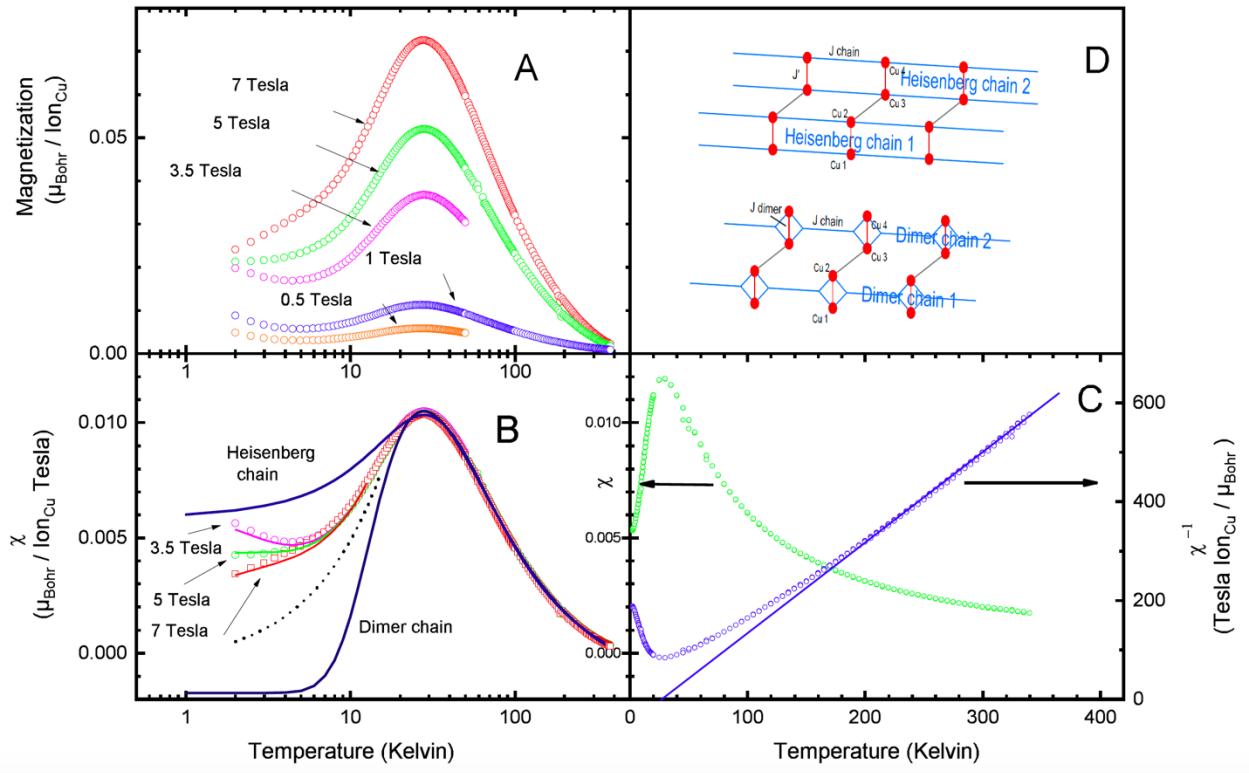

Figure 4. Magnetic response data for TUB75. (A) Magnetization vs. temperature data for TUB75 in different applied magnetic fields. (B) Magnetic susceptibility, χ, (coloured circles) obtained from the magnetization data along with fits (solid blue lines) to the Heisenberg chain and dimer chain models. The upturn in the low-temperature signal (< 10 K), which is suggestive of the presence of paramagnetic impurities, is fit by Brillouin functions (solid coloured lines) with a baseline signal (dotted black line). (C) Magnetic susceptibility (green circles) obtained in a 5 T magnetic field, corrected for the diamagnetic background, and the inverse susceptibility (purple circles) on which a Curie-Weiss high-temperature linear fit is shown (solid purple line). (D) Schematic pictures of Heisenberg chains and dimer chains, the models used to fit the magnetic susceptibility data. See Supporting Information for details.

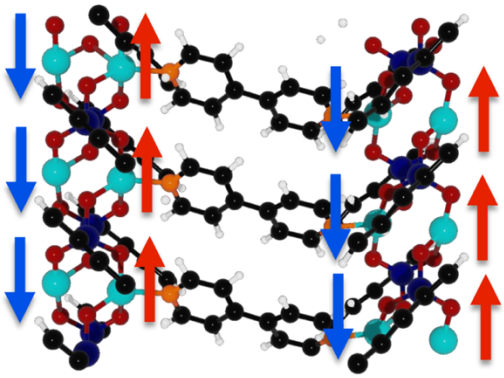

Figure 5. Minimum energy structure of the 1x3x1 supercell depicting the antiferromagnetic configuration of the electrons on each copper (α-spin: red, β-spin: blue). Color definitions: O – red; N – orange; Cu – cyan; C – black; P – blue; H – white.

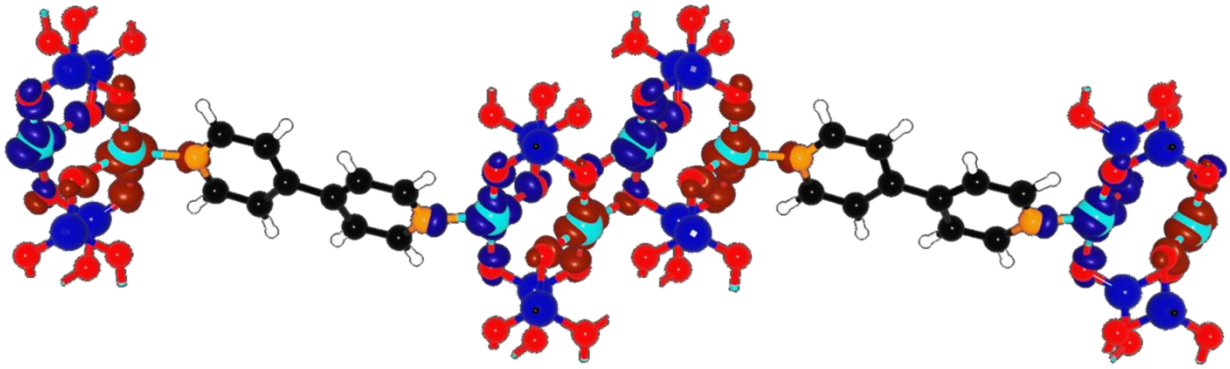

Fig. 6. Spin density iso-surface of a portion of the IBU. β/α spin density is shown in blue/red and corresponds to a difference between the spin-up and spin-down density of 0.005 electrons per $Å^3$. Color definitions: O – red; N – orange; Cu – cyan; C – black; P – blue; H – white.

The first semiconductive metal organic framework (known as TUB75) derived from arylphosphonic acids and a depiction of its antiferromagnetic one-dimensional inorganic building unit composed of a zig-zag chain of corner-sharing copper dimers.

Keyword

Semiconductive MOFs; Magnetic MOFs; DFT calculations; Electrodes; Supercapacitors

Title

Phosphonate metal-organic frameworks: A novel family of semiconductors

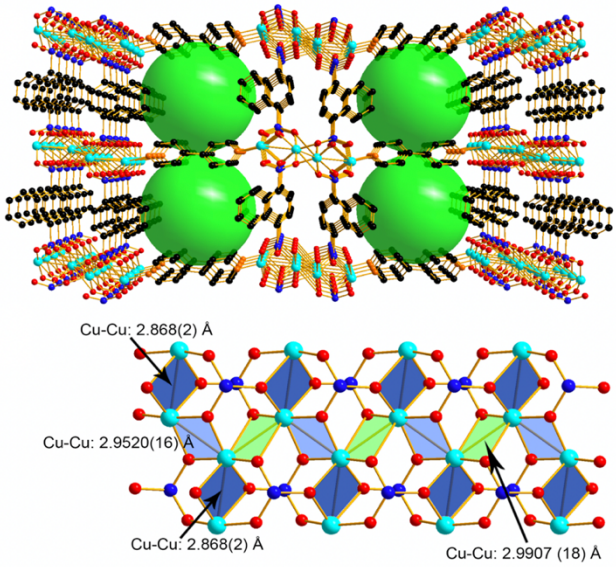

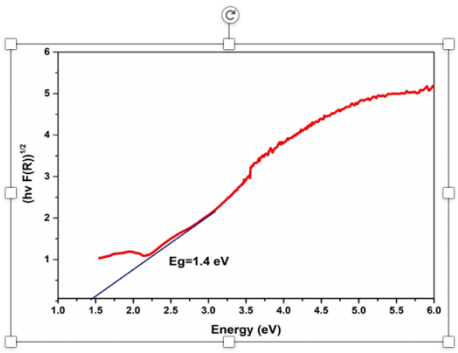

Supporting Information

Phosphonate metal-organic frameworks: A novel family of semiconductors

Konrad Siemensmeyer, Craig A. Peeples, Patrik Tholen, Bünyemin Çoşut, Gabriel Hanna, Gündoğ Yücesan**

Density functional theory calculations

All of the density functional theory (DFT) calculations on TUB75 were performed with the Amsterdam Density Functional BAND (ADF2018) package.[1,2] Since TUB75 is a bulk material, periodic boundary conditions were applied to a 1x3x1 supercell (with unit cell lattice parameters of a=17.907 Å, b=13.931 Å, c=10.086 Å) containing six copper dimers and the associated organic linkers (see Figure S3). All wave functions were expanded using atomic Slater-type orbital (STO) basis sets, which are all-electron basis sets and are more similar to "real" atomic orbitals than plane-wave basis sets (avoiding the use of pseudo-potentials and effective core potentials). A geometry optimization of the experimental crystal structure[3] was performed with the lattice vectors set to their experimental values. The optimization was done using the fast inertial relaxation engine (FIRE)[4] algorithm and spin-polarized, unrestricted Kohn-Sham[5,6] DFT (as each Cu^{2+} has an unpaired electron) at the PBE[7]-D3-BJ-damping[8-10] level of theory, with a triple-ζ polarized (TZP) STO basis set for the copper atoms and a double-ζ polarized (DZP) STO basis set for the main group atoms, Γ-point sampling, and good numerical quality. Single-point calculations were then performed on the optimized structure using the range-separated hybrid HSE06[11-14] functional to obtain the band gap, exchange energy, AFM spin densities, partial charges, band structure, and projected density of states (pDOS), with basic numerical quality in order to reduce computational time (as HSE06 calculations on such large systems are very costly). Hybrid functionals such as HSE06 are known to more accurately calculate band gaps and describe the electronic structure than the generalized gradient approximation (GGA) functionals.[15,16]

Electronic population analyses of the HSE06-calculated density were performed using the Hirshfeld,[17] Voroni,[18] CM5,[19,20] and Mulliken[21] methods. As seen in Table S2, each O has, on average, less than -0.3 elementary charge units for a total of less than -0.9 elementary

charge units on the three terminating oxygens in 1,4-NDPA. While the partial charges obtained from the various methods differ considerably in magnitude in some cases, the signs are all the same. Together, the results suggest that Cu, P, and H have slightly positive charges, while N, O, and C have slightly negative charges.

The energy of the ferromagnetic (FM) configuration was calculated by enforcing all 12 unpaired electrons on the 12 copper atoms to have α-spins, and the energy of the antiferromagnetic (AFM) configuration was calculated by enforcing 6 α-spins and 6 β-spins.

Magnetization measurements

Magnetization measurements were carried out on a 2.57 mg sample of hand-picked crystals of TUB75 (equivalent to 6.06 μmol Cu ions), which was prepared according to the procedure described by Bulut *et al.*[3] The measurements were performed using a commercial VSM - Squid magnetometer by Quantum Design (QD)[22] with magnetic fields ranging from 50 mT to 7 T and temperatures ranging from 2 K to 380 K. The complete set of raw data will be published online as a citable HZB publication. The sample was filled into a standard QD squid measurement capsule, which is known to generate a diamagnetic background. The magnetometer was operated in DC mode, with the sample signal measured at 200 points along the second-order gradiometer detection coil. To determine the diamagnetic background (for subsequent correction of the signals), two different datasets were collected in 1 T and 5 T fields with an empty capsule.

UV-Vis measurements

A solid-state diffuse reflectance UV-Vis spectrum of hand-picked TUB75 crystals was obtained on a Varian Cary 300 UV-Vis spectrophotometer (see Figure S2). An indirect Tauc plot was generated to extract the optical bandgap (see **Figure 3**B in main text).

Supplementary Text

Magnetic susceptibility fitting

To fit our magnetic susceptibility data, we considered a Heisenberg chain (HC) coupled to *m* other chains. A numerical approximation[23] to the Bonner-Fisher model[24] yields the following expression for the susceptibility of the *S*=½ HC:

$$\chi_{HC} = \frac{3C}{T}\frac{0.25 + 0.14995x + 0.30094x^2}{1 + 1.9862x + 0.68854x^2 + 6.0626x^3} + \frac{C_{Para}}{T-\theta} + c_{Dia} \quad (1)$$

where

$$x = \frac{J_{Chain}}{kT} \quad (2)$$

T is the temperature, and the Curie constant (in units of μ_B/ion) is

$$C = \frac{n\mu_B g^2 s(s+1)}{3k_B} \quad (3)$$

In the above equation, *n* is the number of Cu ions per formula unit and is treated as a fitting parameter. The magnetic susceptibility, taking into account the interaction with the *m* other chains, is given by [23]

$$\chi_m = \frac{\chi_{HC}}{1 - \frac{2mJ'\chi_{HC}}{n\mu_B g^2}} \quad (4)$$

where J' is the inter-chain interaction. The best fit was obtained with a double chain (i.e., m=1), J_{chain} = 16.8 K, J' = -22 K, and a value of n that suggests the presence of two such double chains, i.e., two independent HC's as depicted in Figure 2B of the main text.

We also considered the dimer chain model to fit the magnetic susceptibility data. For this model, the magnetic susceptibility is given by [25,26]

$$\chi_{DC} = \frac{3C}{T\left(3 + Exp\left(\frac{J_{Dimer}}{k_B T}\right) + \frac{J_{Chain}}{k_B T}\right)} + \frac{C_{Para}}{T - \theta} + \chi_{Dia} \quad (5)$$

where the Curie constant, C, is given by Equation 3, χ_{dia} is a constant diamagnetic term, and C_{para} is the paramagnetic impurity term.

The best fit to the data above 10 K was obtained with J_{dimer} = 54 K and J_{chain} = -2.6 K. We found that the value of J_{dimer} was quite stable with respect to changes within the fitted (temperature) range, whereas the value of J_{chain} depended somewhat on the dataset and fitted (temperature) range. Below 10 K, the susceptibility remains finite and positive, while the fit yields small negative values. A Curie constant was obtained with g = 2, n = 2 Cu ions per formula unit, and S = ½.

A Curie-Weiss fit to the high temperature portion of the inverse magnetic susceptibility is shown in Figure 4C of the main text. Given Cu^{2+} spins with S= ½ and g=2, we find from the Curie-Weiss constant that 80% of the Cu^{2+} ions in TUB75 contribute to the high-temperature paramagnetic signal. The Curie temperature is found to be T_C = 25 K, above which the material becomes paramagnetic.

References

[1] G. te Velde, F. M. Bickelhaupt, E. J. Baerends, C. Fonseca Guerra, S. J. A. van Gisbergen, J. G. Snijders, T. Ziegler, Chemistry with ADF. *J. Comput. Chem.* 2001, 22, 931.

[2] E. J. Baerends, T. Ziegler, A. J. Atkins, J. Autschbach, D. Bashford, O. Baseggio, A. Bérces, F. M. Bickelhaupt, C. Bo, P. M. Boerritger, L. Cavallo, C. Daul, D. P. Chong, D. V Chulhai, L. Deng, R. M. Dickson, J. M. Dieterich, D. E. Ellis, M. van Faassen, A. Ghysels, A. Giammona, S. J. A. van Gisbergen, A. Goez, A. W. Götz, S. Gusarov, F. E. Harris, P. van den Hoek, Z. Hu, C. R. Jacob, H. Jacobsen, L. Jensen, L. Joubert, J. W. Kaminski, G. van Kessel, C. König, F. Kootstra, A. Kovalenko, M. Krykunov, E. van Lenthe, D. A. McCormack, A. Michalak, M. Mitoraj, S. M. Morton, J. Neugebauer, V. P. Nicu, L. Noodleman, V. P. Osinga, S. Patchkovskii, M. Pavanello, C. A. Peeples, P. H. T. Philipsen, D. Post, C. C. Pye, H. Ramanantoanina, P. Ramos, W. Ravenek, J. I. Rodríguez, P. Ros, R. Rüger, P. R. T. Schipper, D. Schlüns, H. van Schoot, G. Schreckenbach, J. S. Seldenthuis, M. Seth, J. G. Snijders, M. Solà, S. M., M. Swart, D. Swerhone, G. te Velde, V. Tognetti, P. Vernooijs, L. Versluis, L. Visscher, O. Visser, F. Wang, T. A. Wesolowski, E. M. van Wezenbeek, G. Wiesenekker, S. K. Wolff, T. K. Woo, A. L. Yakovlev, ADF2018, SCM, Theoretical Chemistry, Vrije Universiteit, Amsterdam, The Netherlands, https://www.scm.com (**2018**).

[3] A. Bulut, Y. Zorlu, M. Wörle, A. Çetinkaya, H. Kurt, B. Tam, A. Ö. Yazaydın, J. Beckmann, G. Yücesan, Short naphthalene organophosphonate linkers to microporous frameworks. *ChemistrySelect*. **2017**, 2, 7050.

[4] E. Bitzek, P. Koskinen, F. Gähler, M. Moseler, P. Gumbsch, Structural relaxation made simple. *Phys. Rev. Lett.* **2006**, 97, 170201-1

[5] U. Von Barth, L. Hedin, A local exchange-correlation potential for the spin polarized case. I. *J. Phys. C Solid State Phys.***1972**, 5, 1629

[6] C. R. Jacob, M. Reiher, Spin in density-functional theory. *Int. J. Quantum Chem.* **2012**, 112, 3661.

[7] J. Perdew, K. Burke, M. Ernzerhof, Generalized gradient approximation made simple. *Phys. Rev. Lett.* **1996,** 77, 3865.

[8] S. Grimme, J. Antony, S. Ehrlich, H. Krieg, A consistent and accurate ab initio parametrization of density functional dispersion correction (DFT-D) for the 94 elements H-Pu. *J. Chem. Phys.* **2010**, 132, 154104-1.

[9] S. Grimme, S. Ehrlich, L. Goerigk, Effect of the damping function in dispersion corrected density functional theory. *J. Comput. Chem.* **2011**, 32, 1456.

[10] J. P. Perdew, A. Ruzsinszky, G. I. Csonka, O. A. Vydrov, G. E. Scuseria, L. A. Constantin, X. Zhou, K. Burke, Restoring the density-gradient expansion for exchange in solids and surfaces. *Phys. Rev. Lett.* **2008**, 100, 136406-1

[11] J. Heyd, G. E. Scuseria, M. Ernzerhof, Hybrid functionals based on a screened Coulomb potential. *J. Chem. Phys.* **2003**, 118, 8207.

[12] J. Heyd, G. E. Scuseria, Efficient hybrid density functional calculations in solids: Assessment of the Heyd-Scuseria-Ernzerhof screened Coulomb hybrid functional. *J. Chem. Phys.* **2004**, 121, 1187.

[13] J. Heyd, G. E. Scuseria, M. Ernzerhof, Erratum: Hybrid functionals based on a screened Coulomb potential. *J. Chem. Phys.* **2006**, 124, 219906

[14] A. V. Krukau, O. A. Vydrov, A. F. Izmaylov, G. E. Scuseria, Influence of the exchange screening parameter on the performance of screened hybrid functionals. *J. Chem. Phys.* **2006**, 125, 224106-1

[15] Á. Morales-García, R. Valero, F. Illas, An empirical, yet practical way to predict the band gap in solids by using density functional band structure calculations. *J. Phys.*

Chem. C. **2017**, 121, 18862.

[16] M. G. Goesten, R. Hoffmann, Mirrors of bonding in metal halide perovskites. *J. Am. Chem. Soc.* **2018**, 140, 12996.

[17] F. L. Hirshfeld, Bonded-atom fragments for describing molecular charge densities. *Theor. Chim. Acta*. **1977**, 44, 129

[18] C. Fonseca Guerra, J. W. Handgraaf, E. J. Baerends, F. M. Bickelhaupt, Voronoi deformation density (VDD) charges: Assessment of the Mulliken, Bader, Hirshfeld, Weinhold, and VDD methods for charge analysis. *J. Comput. Chem.* **2004**, 25, 189.

[19] A. V. Marenich, S. V. Jerome, C. J. Cramer, D. G. Truhlar, Charge model 5: An extension of Hirshfeld population analysis for the accurate description of molecular interactions in gaseous and condensed phases. *J. Chem. Theory Comput.* **2012**, 8, 527

[20] C. A. Peeples, G. Schreckenbach, Implementation of the SM12 solvation model into ADF and comparison with COSMO. *J. Chem. Theory Comput.* **2016**, 12, 4033.

[21] R. S. Mulliken, Electronic population analysis on LCAO-MO molecular wave functions. I. *J. Chem. Phys.* **1955**, 23, 1833.

[22] VSM - Squid MPMS3 by Quantum Design, USA.

[23] W. E. Hatfield, R. R. Weller, J. W. Hall, Exchange coupling in the sulfur-bridged quasi-linear-chain compound bis(dimethyldithiocarbamato)copper(II). Observations on exchange in sulfur-bridged copper(II) compounds. *Inorg. Chem.* **1980**, 19, 3825.

[24] J. C. Bonner, M. E. Fisher, Linear magnetic chains with anisotropic coupling. *Phys. Rev.* **1964**, 135.

[25] E. S. Klyushina, A. T. M. N. Islam, J. T. Park, E. A. Goremychkin, E. Wheeler, B. Klemke, B. Lake, Hamiltonian of the S= 1/2 dimerized antiferromagnetic-ferromagnetic quantum spin chain $BaCu_2V_2O_8$. *Phys. Rev. B*. **2018**, 98.

[26] S. Eggert, I. Affleck, M. Takahashi, Susceptibility of the spin 1/2 Heisenberg antiferromagnetic chain. *Phys. Rev. Lett.* **1994**, 73, 332.

Figures

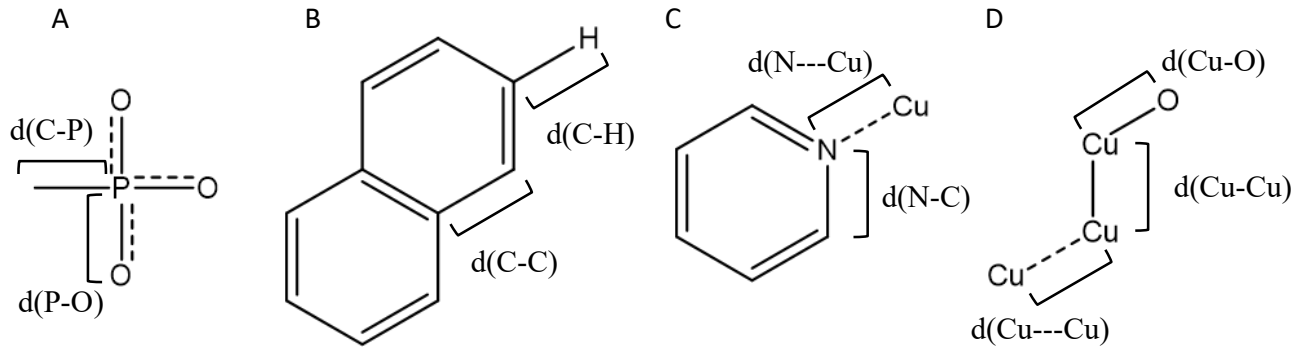

Figure S1. Schematic depicting key inter-atomic separations (distances given in Table S1) in **A)** phosphonic acid group, **B)** naphthalene group, **C)** bipyridine group, and **D)** copper chain.

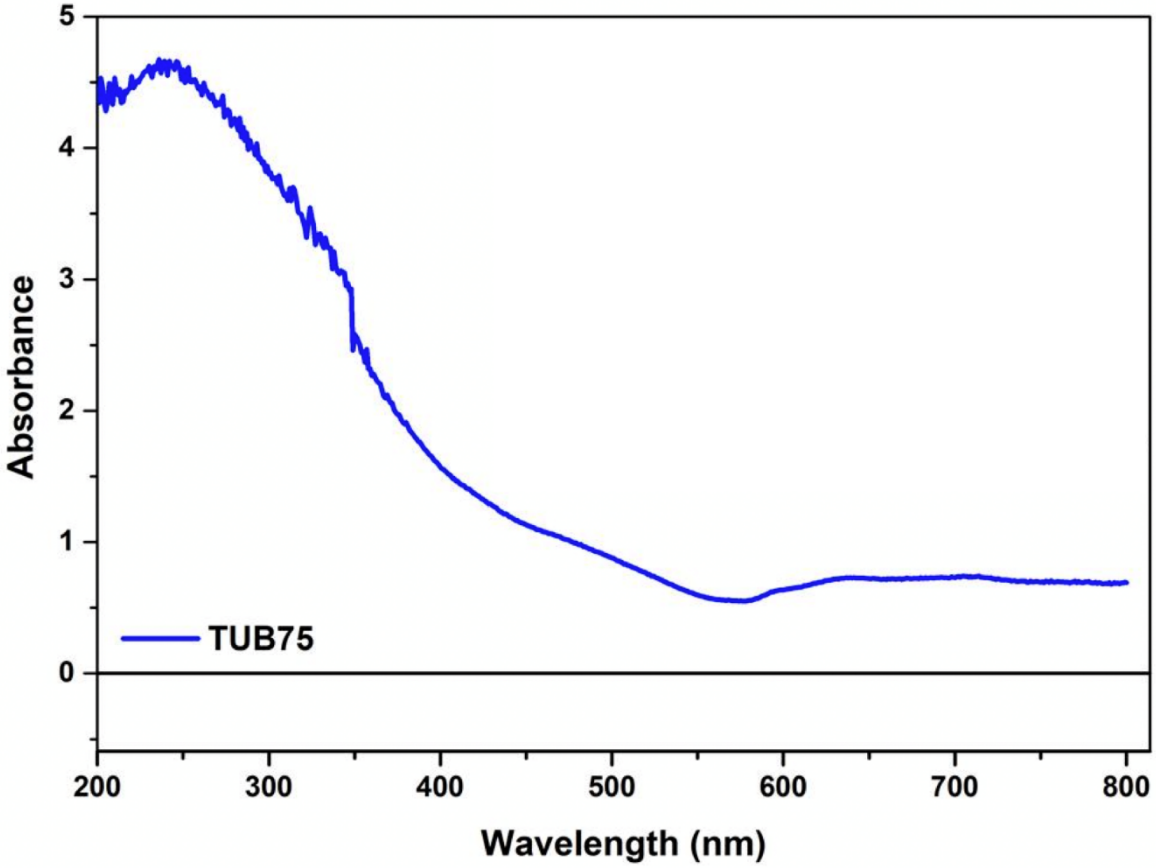

Figure S2. UV-Vis absorption spectrum of TUB75.

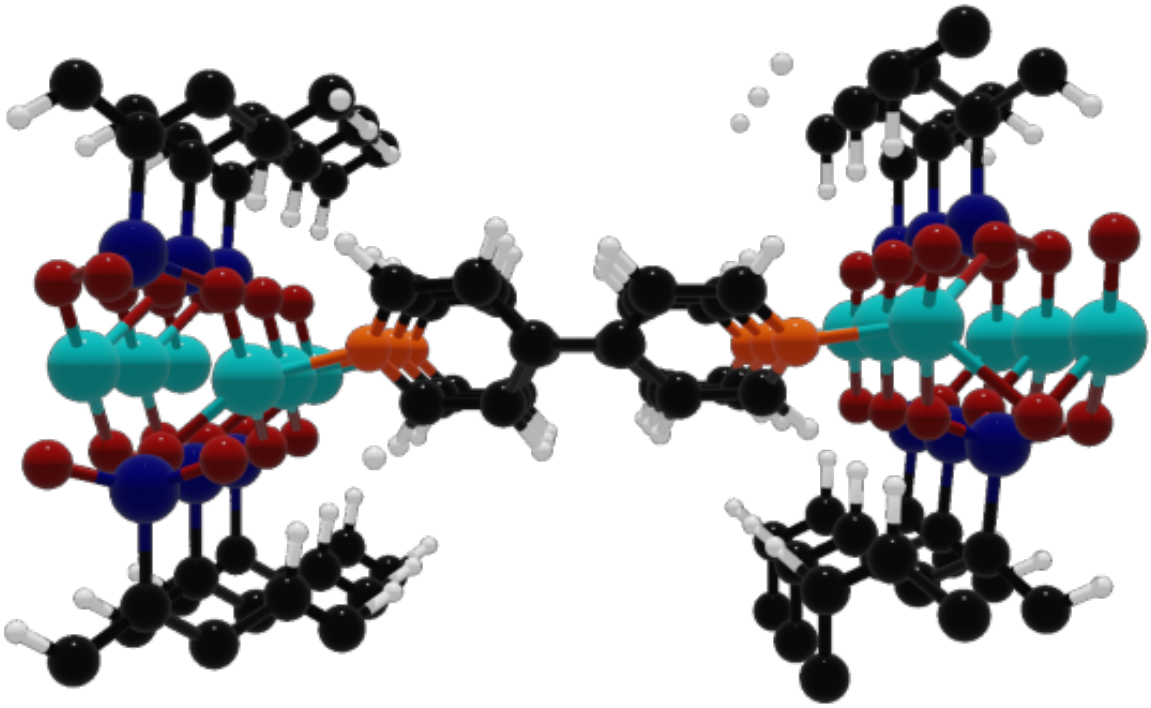

Figure S3. Top-down view of optimized AFM structure of the 1x3x1 supercell obtained at the PBE-D3-BJ level of theory.

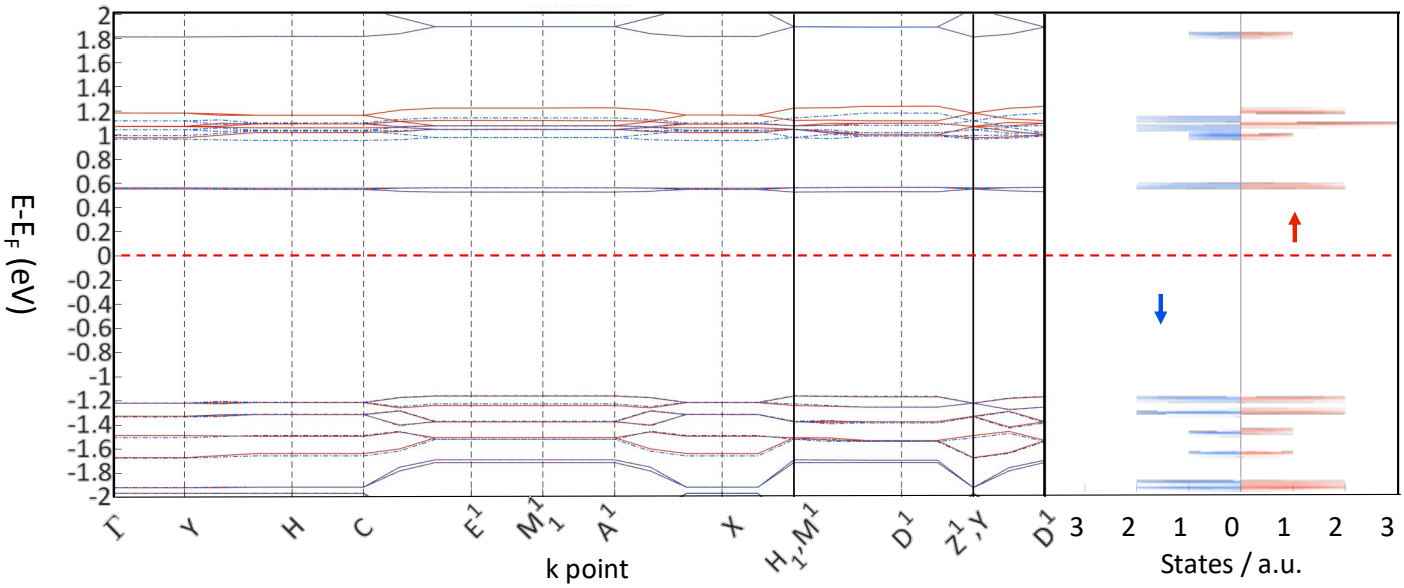

Figure S4. (Left) Band structure of TUB75. The dashed blue and red solid lines correspond to the spin down and spin up contributions, respectively. **(Right)** The corresponding total density of states for spin up (red) and spin down (blue).

Atom Pair	Experimental	Calculated
Figure S1 A		
C-P	1.81 (0.001)	1.83 (0.006)
P-O	1.53 (0.01)	1.56 (0.013)
Figure S1 B		
C-C	1.40 (0.051)	1.41 (0.024)
C-H	0.93 (0.001)	1.09 (0.007)
Figure S1 C		
Cu-N	2.02 (0.001)	2.03 (0.007)
N-C	1.33 (0.027)	1.35 (0.001)
Figure S1 D		
Cu-O	2.06 (0.148)	1.97 (0.03)
Cu-Cu	2.74 (0.000)	2.78 (0.002)
Cu --- Cu	2.97 (0.020)	2.84 (0.108)

Table S1. Comparison of experimental and calculated average inter-atomic distances (in Å) in TUB75. Standard deviations in distances are given in brackets. The calculated structure was obtained from a geometry optimization of the experimental crystal structure at the PBE-D3-BJ TZP/DZP level of theory.

Atom	Hirshfeld[17]	Voroni[18]	CM5[19,20]	Mulliken[21]
Cu	0.536	0.561	0.867	0.921
N	-0.090	-0.126	-0.369	-0.626
O	-0.331	-0.376	-0.434	-0.836
P	0.456	0.484	0.393	1.858
C	-0.022	-0.030	-0.043	-0.083
H	0.039	0.073	0.105	0.131

Table S2. Average partial charges obtained using several electronic population analysis techniques.